SOFT ROBOTS

A compact DEA-based soft peristaltic pump for power and control of fluidic robots

Siyi Xu[1]*, Cara M. Nunez[1,2], Mohammad Souri[1], Robert J. Wood[1]*

Fluid-driven robotic systems typically use bulky and rigid power supplies, considerably limiting their mobility and flexibility. Although various forms of low-profile soft pumps have been demonstrated, they either are limited to specific working fluids or generate limited flow rates or pressures, making them ill-suited for widespread robotics applications. In this work, we introduce a class of centimeter-scale soft peristaltic pumps for power and control of fluidic robots. An array of high power density robust dielectric elastomer actuators (DEAs) (each weighing 1.7 grams) were adopted as soft motors, operated in a programmed pattern to produce pressure waves in a fluidic channel. We investigated and optimized the dynamic performance of the pump by analyzing the interaction between the DEAs and the fluidic channel with a fluid-structure interaction finite element model. Our soft pump achieved a maximum blocked pressure of 12.5 kilopascals and a run-out flow rate of 39 milliliters per minute with a response time of less than 0.1 second. The pump can generate bidirectional flow and adjustable pressure through control of drive parameters such as voltage and phase shift. Furthermore, the use of peristalsis makes the pump compatible with various liquids. To illustrate the versatility of the pump, we demonstrate mixing a cocktail, powering custom actuators for haptic devices, and performing closed-loop control of a soft fluidic actuator. This compact soft peristaltic pump opens up possibilities for future on-board power sources for fluid-driven robots in a variety of applications, including food handling, manufacturing, and biomedical therapeutics.

INTRODUCTION

Fluid-driven soft robots have been developed for a variety of applications, including rehabilitative and therapeutic tools (*1*, *2*), soft grippers and manipulators (*3*–*6*), microfluidic devices (*7*, *8*), and artificial muscles (*9*–*12*). Many of these robots are powered by pressurized liquids and have demonstrated high performance in a variety of working conditions (*13*–*16*). These fluidic machines made of compliant materials have achieved functions that are challenging for conventional rigid systems owing to the properties of the constituent materials. For example, soft grippers can manipulate delicate objects without fear of applying large stresses (*17*), and wearable devices made of flexible or stretchable materials can safely interact with humans and natural systems (*18*, *19*). Despite the widespread use of soft fluidic systems and their functional advantages, there has been a lack of focus on energy sources that match their size, weight, and material properties. Thus far, conventional power sources such as pumps and compressors are the most common approach to drive fluidic actuators. These systems are typically bulky and heavy relative to the actuators they work with, limiting the mobility and adaptability of the robotic systems. Battery-driven microcompressors and miniature pumps can be options for actuators requiring low pressure or flow, but they are composed of rigid components and thus are not ideal for applications requiring compliance throughout the device. Rigid fluidic power supplies can be attached to soft actuators via a tether, but this would limit the mobility of the system. Chemical reactions are another solution for onboard power for soft robots (*20*, *21*), but controlling the reaction rate and the safety of the reactant storage are potential concerns for applications such as wearable robots. Low–boiling point liquids may be used for actuation (*22*, *23*). However, the liquid phase transition in response to a temperature change in the environment could take hundreds of seconds, which cannot provide sufficient bandwidth for cyclic actuation. Given these concerns, compliant and lightweight energy sources are in great need to achieve future onboard power and control of fluidic systems.

The performance requirements for fluidic power systems vary depending on the application. In our work, we target the development of pumps for soft robots; robotics is one of the most challenging uses because both high pressures and precise control of flow (for precision motion or manipulation, for example) are typically necessary. A desirable soft pump for robotic actuators should meet the following guidelines. First, micro- and macroscale fluidic actuators that have been developed in previous research have internal volumes ranging from hundreds of microliters to tens of milliliters, and their actuation time constants could range from 2 to 20 s (*5*, *24*–*26*). To drive these actuators with appropriate bandwidths, a soft pump should be able to generate flows with a pressure of at least 10 kPa and provide a flow rate no less than 6 ml min^{-1} while maintaining a comparable size and weight to the corresponding actuator(s). In addition to generating sufficient pressure, a soft pump with controllable pressure, flow rate, and flow direction is preferable. Such properties will enable high-precision control of end effectors without requiring valves in fluidic circuits, reducing the complexity of the power and control system. Furthermore, the working liquids and their properties could vary depending on the task. These liquids can vary from nutrients and medications for therapeutic purposes to juices for food production and water for wearable and assistive devices. Soft pumps that are compatible with commonly seen fluids with dynamic viscosities in the range

[1]Harvard John A. Paulson School of Engineering and Applied Sciences, Harvard University, Cambridge, MA, USA. [2]Sibley School of Mechanical and Aerospace Engineering, Cornell University, Ithaca, NY, USA.
*Corresponding author. Email: sxu1@g.harvard.edu (S.X.); rjwood@seas.harvard.edu (R.J.W.)

of 0.89 cP (water) (*27*) to 200 cP (syrup) (*28*) are desirable to expand the range of applications.

Various forms of liquid-based soft pumps have been studied in previous research. Microfluidic peristaltic membrane pumps driven by compressed air (*29*), electrostatic forces (*30*, *31*), and thermally responsive materials (*32*) have been developed. Although these pumps have demonstrated reliable pumping for fluidic systems with microscale channels, their flow rates are generally in the range of nanoliters to microliters per minute—insufficient for macroscale actuators and soft robots.

Large-scale soft pumps have also been investigated to drive soft actuators. Electrically responsive dielectric elastomer actuator pumps (*33*, *34*) are able to generate a liquid flow rate of 900 ml min^{-1}. However, they are limited by the maximum output pressure, which to date has been lower than 3 kPa. A lightweight electro-hydrodynamic pump capable of pumping liquid and powering a soft actuator has been developed (*24*, *35*). Because of the pump's operation mechanism, the working liquids are limited to dielectric fluids, and the operation voltage is high (>10 kV). A high-performance elastomeric magneto-hydrodynamic pump has recently been created (*36*). Although the solenoid-driven pump shows reliable blocked pressure and run-out flow rate, a magnetic core coated with ferrofluids is embedded in the fluid channel and thus could potentially contaminate the working liquid.

Peristaltic pumps can be compatible with requirements for high purity because the soft channel is the only component within the pump that comes into contact with the working liquid (*37*). This property prevents contamination of the working liquid caused by exposure to other pump components. Peristaltic pumps can also deliver liquids with a wide range of viscosities, particle-liquid suspensions, or shear-sensitive fluids such as blood, which are challenging for other types of pumps, such as gear pumps or diaphragm pumps, because of their working mechanisms. In addition, peristaltic pumps have a modular design, which allows rapid construction, easy repair, and customization. These properties make soft peristaltic pumps not only appropriate for robotic actuation but also desirable for food handling, wearable haptic devices, compression suits, drug delivery, blood transfer, and implantable pumps, where form factor, compliance, and biocompatibility are critical factors (*37*–*41*).

Macroscale soft peristaltic pumps have been developed in previous research for large pressures and flow rates (*42*, *43*). A powerful peristaltic pump that can generate 40 kPa of pressure and up to 2200 ml min^{-1} of flow rate has been developed (*42*), but its scale (56 cm long and 3 cm in diameter) and mass (over 1.3 kg) far exceed those of many existing fluidic actuators. In addition, rigid air compressors are still required to power the pump. One of the biggest challenges for existing peristaltic pumps for the aforementioned applications is reducing the pump dimensions and weight for wearable or implantable devices while maintaining sufficient mechanical output. This is primarily due to the lack of small-scale lightweight motors, which are the key components in existing peristaltic pumps.

In this work, we present an electrically responsive dynamic dielectric elastomer actuator (DEA) peristaltic pump at centimeter scale for soft robots (Fig. 1A). We used power-dense DEA units operated in a programmed sequence to generate peristaltic movement on the soft channel for liquid pumping. These small form factor DEAs serve as soft motors, providing a solution for low-profile and low-weight peristaltic pumps. Our soft peristaltic pump achieved a maximum blocked pressure of 12.5 kPa with a run-out flow rate of 39 ml min^{-1} and a response time less than 0.1 s. Furthermore, the proposed pump can generate bidirectional flow and tunable output pressure by modulating the DEA electrical inputs such as phase shift and voltage. We also present a finite element model that investigated fluid-structure interactions between the DEAs and the working liquid under different operating conditions and to assist in optimizing the pump functionality. In addition, the peristaltic operation makes the pump compatible with various working liquids, allowing it to serve as a fluidic power source for applications beyond robotic actuation. Our peristaltic pump shows comparable functionalities to other types of non-peristalsis soft pumps developed so far and additionally maintains a low

Table 1. Pump property comparison. MHD, magnetohydrodynamic; EHD, electrohydrodynamic.

Pump type	Pump name	Weight (g)	Voltage (kV)	Power consumption (W)	Pressure (kPa)	Flow rate (ml/min)	Fluidic power density* (W/kg)
Peristaltic pump	DEA pump (this work)	12–15	1.7	3.3	12.5	39	0.27
	Bowel peristalsis pump (*42*)	1356	Pneumatic	/	40	2200	0.54
	Swallowing robot (*43*)	1200	Pneumatic	/	32.5	600	0.26
MHD pump	Elastomeric solenoid-driven pump (*36*)	30	0.001	0.17	8	320	0.7
EHD pump	Stretchable pump (*24*)	1	up to 10	0.1	15	6	0.71
	Self-healing pump (*35*)	3	12–16	3.6	9.2	423	10.8
Diaphragm pump	DE snap-through pump (*33*)	/	5	/	0.6	169.5	/
Commercial solenoid pump	HAWE HR080	4000	0.23	190–300	21,000	550	24.11
	TCS M200 Series	11–13	0.015	0.3	23	330	4.87

*The fluidic power density is calculated as half of the product of the pressure and the flow rate over mass: (pressure · flow rate)/(2 · mass).

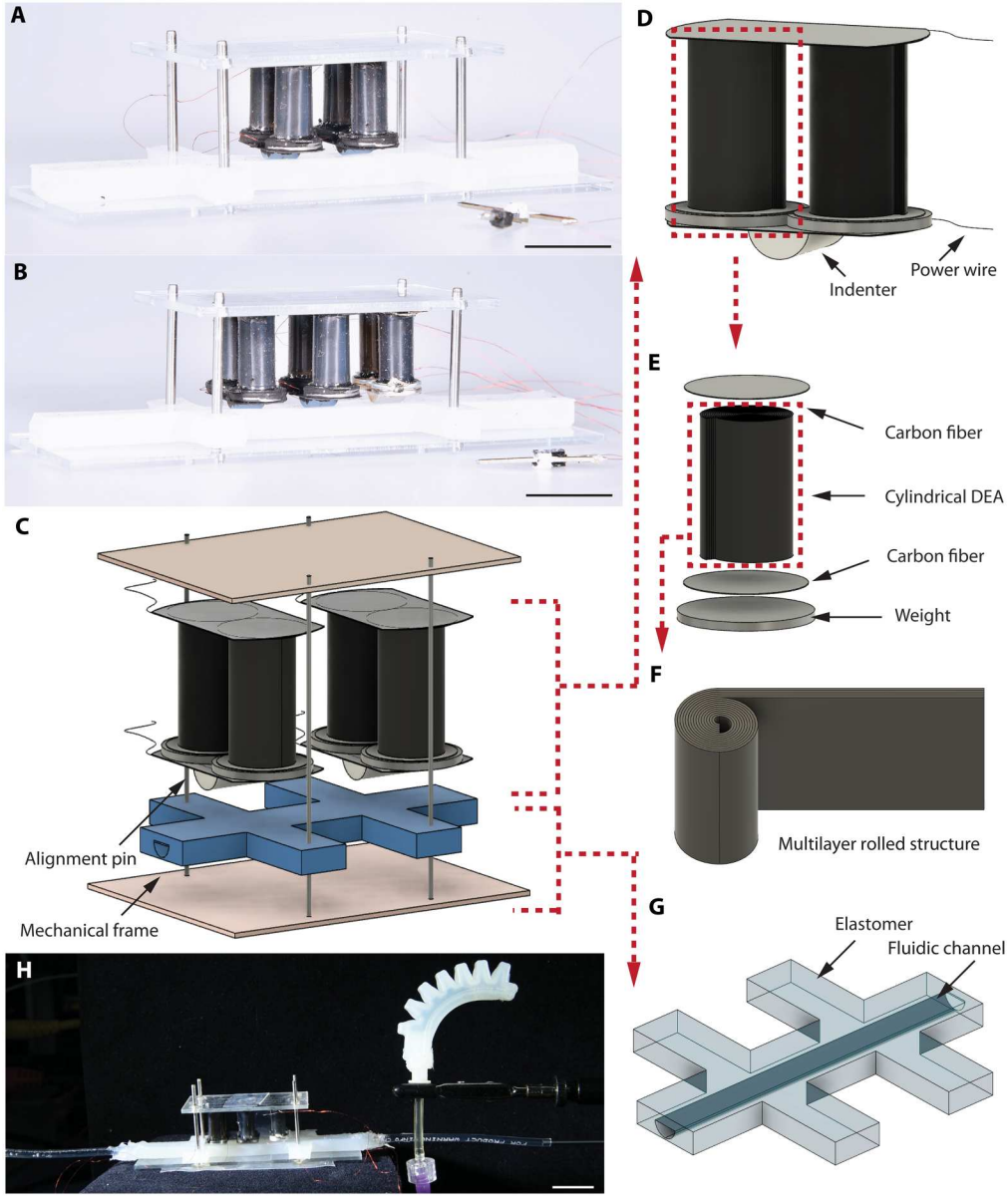

Fig. 1. Design, fabrication, and demonstration of a soft peristaltic pump. Images of (**A**) dual- and (**B**) triple-DEA structure pumps. (**C**) Schematic of a dual-DEA pump. The pump contains a mechanical frame, two DEAs, and a fluidic channel. Magnified schematics of the DEA structures and the channel are shown in (**D**) and (**E**). Each actuator contains two rolled DEAs connected by carbon fiber plates at the two ends. (E) Each rolled DEA contains an elastomeric cylindrical roll, carbon fiber caps, and a weight attached to the free end of the actuator. (**F**) The rolled elastomeric actuator was fabricated from a multilayer DEA sheet. (**G**) A magnified schematic of the fluidic channel. The concave-shaped channel is embedded in an elastomer substrate. Alignment pins pass through the protruding elastomeric areas to align the channel with the DEAs. (**H**) A triple-DEA pump driving a bellow-shaped hydraulic actuator. Scale bars, 1 cm.

profile and similar weight to the actuators it controls (approximately 9 g). A comparison of the performance of off-the-shelf compressors, representative macroscale soft pumps, and our peristaltic pump is shown in Table 1. With these properties, we demonstrate the pump's capabilities as a drink mixer, a power source for finger-like bellows actuators, and wearable haptic devices. We also achieved reliable closed-loop control of the bellows actuator bending motions, demonstrating the potential for the pump to serve as both power source and controller for future integrated soft robots.

RESULTS

Peristaltic pump design and demonstration

The design of our soft pump follows a typical linear peristaltic pump, in which an array of translational actuators periodically deform a section of a straight flexible channel to transport fluid. To create peristaltic flow, the soft pump was constructed with an array of two or more DEA structures, a soft channel, and a mechanical frame (Fig. 1, A to G, and fig. S1). A DEA structure contained two rolled DEAs combined in parallel, with each DEA consisting of sequentially layered carbon nanotube electrodes and elastomer

sheets (*44*, *45*). Two or more DEAs were aligned in parallel and mounted to the top plate of the mechanical frame, with their free ends in contact with the channel via indenters. The channel was adhered to the bottom plate of the frame, which was connected to the top plate through four alignment pins. The mechanical frame supported the DEAs and provided reaction forces when operating the pump. We showed in the previous work (*45*) that the frame could be made of either rigid or compliant materials without affecting the DEA-channel interactions. In this paper, we demonstrated peristaltic pumps with a simple rigid frame composed of acrylic plates and metal pins. When the pump was at rest, the DEAs remained static, and no flow was generated in the channel. When sinusoidal voltage signals with programmed phase shifts were applied to the DEAs, they rhythmically compressed the soft channel under Maxwell stress ($P = \varepsilon_0 \varepsilon_r E^2$, where ε_r is the dielectric constant of the elastomer, ε_0 is free space permittivity, and E is the applied electric field), creating a peristaltic movement on the channel wall and pumping the working liquid toward the selected direction.

For the pump to achieve our target pressure (>10 kPa) and flow rate (>6 ml min^{-1}) while minimizing size and weight to be comparable to the fluidic actuators it will drive, the DEAs must have a high energy density (>1 J kg^{-1}) and an appropriate actuation bandwidth (>10 Hz). High actuation speeds (translation of a single DEA) result in large flow rates, but the DEA spacing divided by the actuation period should not exceed the wave speed of the liquid and the channel it is flowing through—this constitutes a major design criterion of the pump. We constructed the DEAs using a low-viscoelasticity and high–dielectric strength silicone material, Elastosil P7670 (Wacker Chemical). From a previous study (*45*), a multilayer rolled DEA made from P7670 silicone exhibited a large quality factor of six and a high breakdown field of 66 V μm^{-1} under AC excitation. Owing to the material properties of silicone, these DEAs reached an estimated energy density of 4.9 J kg^{-1} and had sufficient bandwidth (600 Hz or higher) for the pump goals (*45*). The dimension of the multilayer DEA sheets—and thus the actuation performance—were determined on the basis of the parameters of the load (i.e., channel geometry and materials) as described below.

The soft channel material was chosen to be Dragon Skin 20 (Smooth-on) silicone elastomer. This material could follow the DEA movement up to hundreds of hertz without serious phase distortion. We designed the channel cross section to be a concave shape to minimize back flow (Fig. 1G). The channel cross section was 1 mm deep and 4 mm wide to ensure a sufficient flow rate (>6 ml min^{-1}) while limiting the pressure drop within the channel to be less than 0.3 kPa based on the Hagen-Poseuille equation (*46*).

On the basis of the lumped parameter model discussed in previous work (*45*), a DEA roll made from a 100-mm-long, 210-μm-thick, and 10-mm-tall multilayer sheet was able to fully compress the channel with the aforementioned design. Assuming that the channel elastomer and liquids are incompressible, the pressure from the actuator should be proportional to the pressure in the channel (fig. S2). To magnify the output pressure of the pump, two pairs of cylindrical rolls were combined in parallel to build a dual-DEA architecture to increase the output force and avoid premature electrical breakdown (Fig. 1D) (*47*). We added an additional weight to the DEA free end to tune its resonance to the desired operating frequency (Fig. 1E). Each DEA contacted the soft channel via a 5-mm-long indenter with the same arc shape as the channel cross section adhered to its free end. The fabrication process of the DEAs and the assembly of the pump are detailed in Materials and Methods and fig. S1.

With these selected parameters, we fabricated and studied two types of the peristaltic pumps: a dual-DEA pump (weight, 12 g; length, 5 cm; height, 2 cm) and a triple-DEA pump (15 g, same dimensions). With the dual-DEA pump, we investigated the pump performance with different DEA separation distances and operation phase shifts. With the triple-DEA pump, we demonstrated its compatibility with various liquids and used this pump to power and control a finger-sized bellows actuator and a haptic device (Fig. 1H).

Operation frequency selection and DEA characterization

The DEAs served as soft motors within the pump structure, performing work on the soft channel surface and generating peristaltic wave–like movements. Because our DEAs had a large quality factor, tuning the DEA operating frequency was critical for pump performance. When a DEA deformed the channel, it moved the liquid underneath the indenter both left and right. Although higher operating frequency was likely to move a greater volume per unit time, there were two key factors in determining the proper actuation frequency. First, the phase of the wave relative to the actuator input must be carefully tuned. During peristalsis, the creation of a low-pressure region, allowing fluid to enter the channel, was a critical step to entraining the flow. Second, to achieve efficient pumping, constructive interference between the wave and adjacent actuator inputs was desired. The product of the wave speed and the phase (in seconds) between two adjacent DEAs should match the distance between them. A separation shorter than this would reduce the weight and size of the pump, but this would be suboptimal. In addition, a hard lower separation limit of 10 mm existed because of the actuator diameter.

The wave speed can be estimated on the basis of a string vibration model

$$v = \sqrt{\frac{T_{\text{string}}}{u}} \tag{1}$$

where T_{string} is the tension force in the string, and u is the linear density of the string (fig. S3). Assuming that the mass of the string is the summation of the mass of the elastomer channel wall and the water and that the tension in the string is the elastomer stretching force during deformation, we calculated the wave speed to be approximately 4.3 m s^{-1}. We based the DEA on previous designs and modified the actuator structure with a number of mechanical features specifically to meet the pump criteria. Compared with previous designs, the new DEA cylinder′s height and length were increased to 10 and 100 mm, respectively, to provide sufficient compression to the channel. This geometry change decreased the resonant frequency from 600 to 450 Hz, and each individual DEA weighed approximately 290 mg. Given a wave speed of 4.3 m s^{-1} and a minimum DEA separation of 10 mm, the DEA resonance should be less than 280 Hz.

To maximize the DEA energy output and meet the frequency requirement, we added a weight to the actuator′s free end to shift the resonance to a lower frequency by increasing the DEA′s effective mass (Fig. 2A and movie S1). Theoretically, a taller or a thicker DEA cylinder design should have similar effects. However, a DEA with a

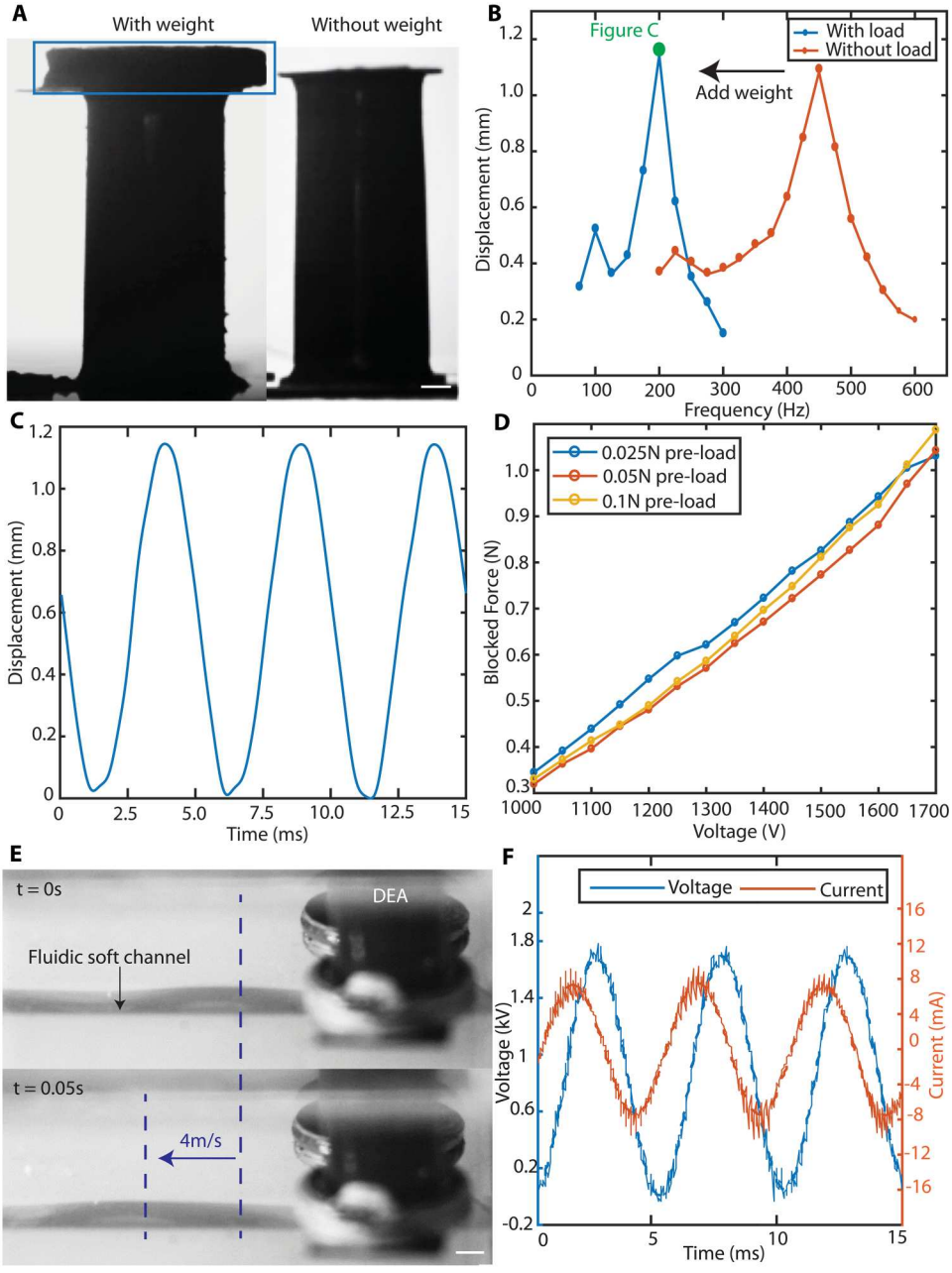

Fig. 2. DEA actuation frequency selection and performance characterization. (**A**) Pictures of a rolled-DEA with and without a weight. (**B**) Free displacement of a single-rolled DEA with and without a weight as a function of frequency, operated at 1400 V. (**C**) Free displacement as a function of time operated at 1400 V and 200 Hz. The labeled point in (B) is the average of the peak-to-peak displacement in (C). (**D**) Blocked force of a DEA structure that consists of two rolled actuators with different preloads. (**E**) Flow in the soft channel captured with a high-speed camera when operating the DEA at 200 Hz and 1400 V. (**F**) Applied voltage and corresponding current when driving a two-roll structure at the optimal condition of 1680 V and 200 Hz. Scale bars, 1 mm.

larger cylinder aspect ratio was more likely to buckle under the same external load, increasing the risk of mechanical failure of the pump. A thicker DEA roll required a larger active area, which could increase the risk of early electrical breakdown. As shown in Fig. 2 (B to D), a 10-mm-tall cylindrical DEA had a resonant free displacement of 1.08 mm at 1000 V and 450 Hz. By adding a 420-mg weight to the free end, we shifted the resonance down to 200 Hz and slightly increased the free displacement to 1.14 mm at 1000 V (because of an increase in the quality factor). This additional weight did not affect the DEA blocked force. The blocked force was proportional to the driving voltage squared and was approximately independent of frequency up to actuator resonance. This was because the DEAs had a much shorter electrical time constant (0.06 ms) compared with their driving period (5 ms). We applied various preloads to the DEAs during characterization, mimicking the loads experienced during operation. In these experiments, the blocked force was the

additional load generated by the DEAs beyond the preload, and it remained relatively consistent under different preloads, as shown in Fig. 2D and fig. S4.

With the reduced resonance of 200 Hz, the maximum actuator separation distance could be up to 21.5 mm based on our wave speed model. We experimentally validated the estimation by driving one DEA at 200 Hz over a soft channel filled with water and observed the channel performance with a high-speed camera (Phantom, V1612, 20,000 fps). At 200 Hz, we estimated a wave traveling speed of approximately 4 m s^{-1} within one oscillation period (Fig. 2E and movie S2), which agreed with our model estimation. With the wave speed and actuator operating frequency determined, we selected the DEA separation distance to be 12 mm. Larger distances were also feasible, but longer fluidic channels would increase the size and weight of the pump. Although we selected a design that met our requirements, there were other tunable parameters in the system, including the actuator and channel design parameters, that provided the ability to adjust the pump performance.

From our previous works (*45*, *48*), the DEAs were robust to millions of cycles operated at 500 Hz and 1800 V. As the operation frequency was reduced to 200 Hz, the DEAs could be safely driven at a maximum voltage of 1680 V and exhibited similar stability and lifetime. The peristaltic pump converted electrical energy first to mechanical energy by deforming the channel, which then transmitted this work to fluid energy in the resulting wave. Compared with the DEAs in previous work, our DEA design required less electrical power and had a higher efficiency because of a reduction in the driving frequency. We used an external circuit to measure the power consumption of a DEA structure. When operated at 1680 V and 200 Hz, the peak-to-peak current requirement for a DEA was approximately 15 mA, and the time-averaged power consumption was 1.16 W (Fig. 2F and fig. S5, A to D). The efficiency of the DEAs was defined as the ratio of their output mechanical power to electrical power consumption. We measured the displacement of the DEA at 1680 V when loaded with the water-filler soft channel with a high-speed camera to be approximately 0.88 mm (fig. S5E). Together with the measured blocked force, the estimated DEA transduction efficiency was approximately 8.3%, close to the efficiency of the DEAs used in our previous work (9%) (*45*). Details of power consumption measurement and efficiency calculation are provided in the Supplementary Materials.

Peristalsis motion analysis and control of a dual-DEA pump

At a drive frequency of 200 Hz, the phase shift of the electrical inputs and the distance between actuators are two key factors that determine the pump performance. Mismatches between phase and distance lead to destructive interference, which strongly influences the pump efficiency. Taking a dual-DEA pump design as an example, we developed a dynamic fluid-structure interaction multiphysics finite element model to investigate the influence of DEA interactions on the fluid flow (Fig. 3 and movie S3). We first formed the pump to be a concave-shaped fluidic channel encapsulated by a silicone sheet as the channel wall (Fig. 3A and fig. S6). The left and right ends of the channel were defined as the inlet and outlet, respectively. To mimic the motion of the DEAs, two rigid indenters were placed on top of the elastomeric wall, and time-varying normal forces equivalent to the DEA blocked force were applied to their top surfaces. The blocked forces were derived from the electrical input based on the model developed in the previous study (*45*), simplifying the mechanical behavior of the DEAs to a mass-spring-damper system (fig. S7). The simulated blocked force agreed well with the measured results, and details are described in the Supplementary Materials. We defined the phase shift of the driving voltage of DEA1 to always be zero and that of DEA2 to be a variable, Φ. Because the DEAs oscillated along their axial directions, we constrained the indenter motion in the two planar directions and only allowed one degree of freedom in the vertical direction. Next, we applied a linear elastic material channel with an added viscoelastic parameter to describe the channel material (silicone) behavior. The liquid flow was modeled as an incompressible laminar flow on the basis of the calculated Reynolds number (1483), estimated with the maximum instantaneous flow rate explained in the previous section (see the Supplementary Materials). Last, we applied boundary and initial conditions to the fluid channel and elastomer sheet. We assumed that the channel outlet and inlet were connected to a large volume of fluid and allowed to freely flow (open boundary conditions). At the initial condition, fluid velocities in all directions were zero, and no external pressure was applied to the liquid. For the elastomer sheet, we constrained the displacement of its side surfaces because they were bonded to the channel substrate in our experiments. The initial velocity and displacement of the sheet were zero. Details of the model assumptions and derivations can be found in the Supplementary Materials.

To evaluate the pump performance, we investigated the modeled average flow rate ($\overline{Q}$) per working cycle (T). The average flow rate was defined as the time average of the integral of the instantaneous flow over the channel cross-sectional area through the outlet per cycle

$$\overline{Q} = \frac{1}{T}\int_0^T \left(\int_S (\vec{q} \cdot \vec{n}) dA \right) dt \tag{2}$$

where $\vec{q}$ is the volumetric flux, and $\vec{n}$ is the unit vector pointing outward.

From the simulation, the pump could generate a maximum flow rate of 25 ml min^{-1} at 1400 V and 200 Hz when the phase shift of DEA2 was around 280° to 290° (Fig. 3B). The average flow rates from 0° to 360° at various DEA separations with an increment of 30° are shown in Fig. 3C. As the phase shift gradually increased or decreased from 280°, the flow rate was reduced and reached zero when Φ equaled 360° or 180°. A further decrease or increase (below 180° or above 360°) would result in flows in the reverse direction, as was indicated by the negative flow rate values. The distance between the two DEAs also affected the pump performance. With the same channel length, increasing the DEA distance would bring the actuator closer to the end of the channel. The "squeezing out" and "pulling in" of water at the inlet and outlet during each working cycle resulted in destructive interference, reducing the maximum outflow rate and shifting the optimal phase shift, Φ.

During each working cycle, DEA1 deformed the channel and generated ripples on both sides of the actuator that traveled in opposite directions. When the travel distance approached the DEA separation distance, DEA2 released the channel and allowed the wave to move forward. As DEA2 compressed the channel, DEA1 followed this motion with a proper delay so that it stopped the back-flow caused by DEA2. A simulation of a dual-DEA pump operated at 1400 V, 200 Hz, and 290° phase shift is shown in Fig. 3 (D and E). Because of the increased hydraulic pressure when stopping

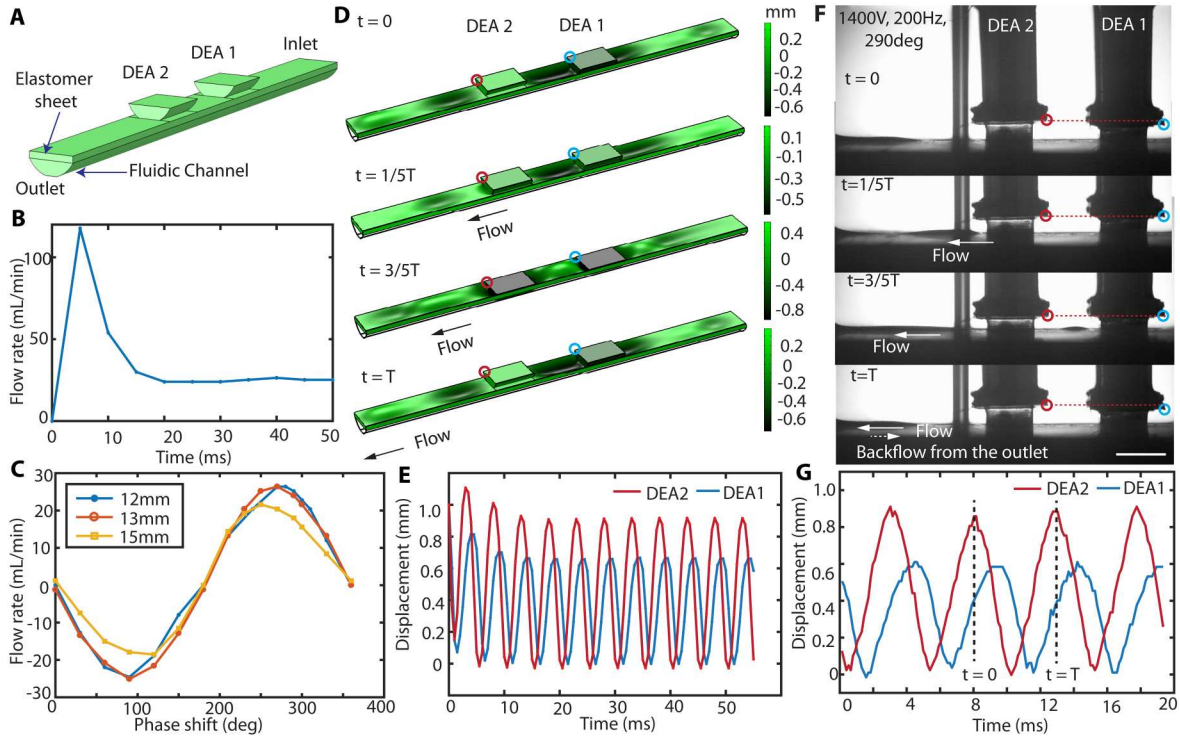

Fig. 3. Fluid-structure interaction FEA of a dual-DEA pump and experimental validation. (**A**) Schematic of the setup of the FEA model. The DEAs are simplified to two indenters attached to the channel wall. (**B**) Simulated average flow rate per working cycle when operating the pump at 1400 V and 200 Hz. The phase shift of DEA2 was 290°. (**C**) Simulated average flow rate as a function of phase shift, Φ, and DEA separation at 1400 V and 200 Hz. (**D**) Model of the interactions between the DEAs and the channel within one oscillation cycle at 1400 V and 200 Hz. The legends show the position of the indenters and channel surface relative to their initial positions. (**E**) Simulated displacements at the highlighted blue and red points in (D) of the two DEAs as a function of time. We set the lowest DEA position to be zero displacement. (**F**) Interaction between DEAs and the fluidic channel within one oscillation cycle captured by a high-speed camera. (**G**) Tracked DEA motions [the highlighted red and blue points in (E)] as a function of time. The lowest position was set to be zero displacement. Scale bar, 5 mm.

the wave, the displacement of DEA1 was lower than DEA2 under the same operating conditions. The correct phase between the DEA oscillations reinforced the forward flow and minimized back-flow; thus, the maximum flow rate was achieved. When the phase shift between the DEAs was not 290°, the forward wave was disturbed by DEA2, and the backward wave could not be fully blocked by DEA1, which reduced the accumulated flow within one pump cycle. The extreme case would happen when the phase shift was 0°, 180°, and 360°, where standing waves were generated, and the output rate became zero.

To validate this model prediction, we conducted experiments with a two-DEA pump, driving the DEAs at 1400 V, 200 Hz, and a 290° phase shift, with a 12-mm actuator separation. When operating at a phase shift of 290°, a continuous flow of 27 ml min^{-1} was generated. As we increased the phase shift to 360°, barely any flow could be observed. The motions of the DEAs were extracted from a high-speed video (captured with Phantom V1612 at 20,000 fps) to visualize the interactions between the DEAs and the peristalsis wave on the channel. As shown in Fig. 3 (F and G), as we operated DEA2 with a 290° phase shift, a traveling wave was generated and traveled from DEA1 to DEA2 and then toward the outlet. The tracked motions of the two DEAs also agree well with the model results. These simulations serve to understand the pump behavior, but the results are based on many assumptions and simplifications. Pump performance must be experimentally determined, which we will elaborate on in the following section.

Characterization of pump performance

The pump performance can be modulated by several critical fabrication and design parameters, namely, the pre-indentation depth into the channel, the DEA separation distance, the channel depth, and the number of DEAs within the pump. To characterize the pump behavior, we connected it in parallel with a fluidic pressure sensor and in series with a flow rate meter (Fig. 4A). We defined the measured flow rate with zero outlet resistance to be the run-out flow rate and the pressure when the flow rate approached zero (specifically, when the channel outlet was connected to a high-resistance load) to be the blocked pressure. The pump inlet was inserted into a water reservoir, and its outlet was either open to the air or connected to a mechanical load, such as a hydraulic actuator. The influence of the aforementioned parameters on the pump was studied using the measured run-out flow rate and blocked pressure under various conditions.

During the pump assembly, we pre-indented the elastomer channel with the DEAs so that a reaction force was applied to the DEAs by the channel. This reaction force stabilized the DEAs during their axial oscillations, preventing misalignment and separation between the actuators and the channel during pump operation. With a deeper pre-indentation, the channel was compressed to a

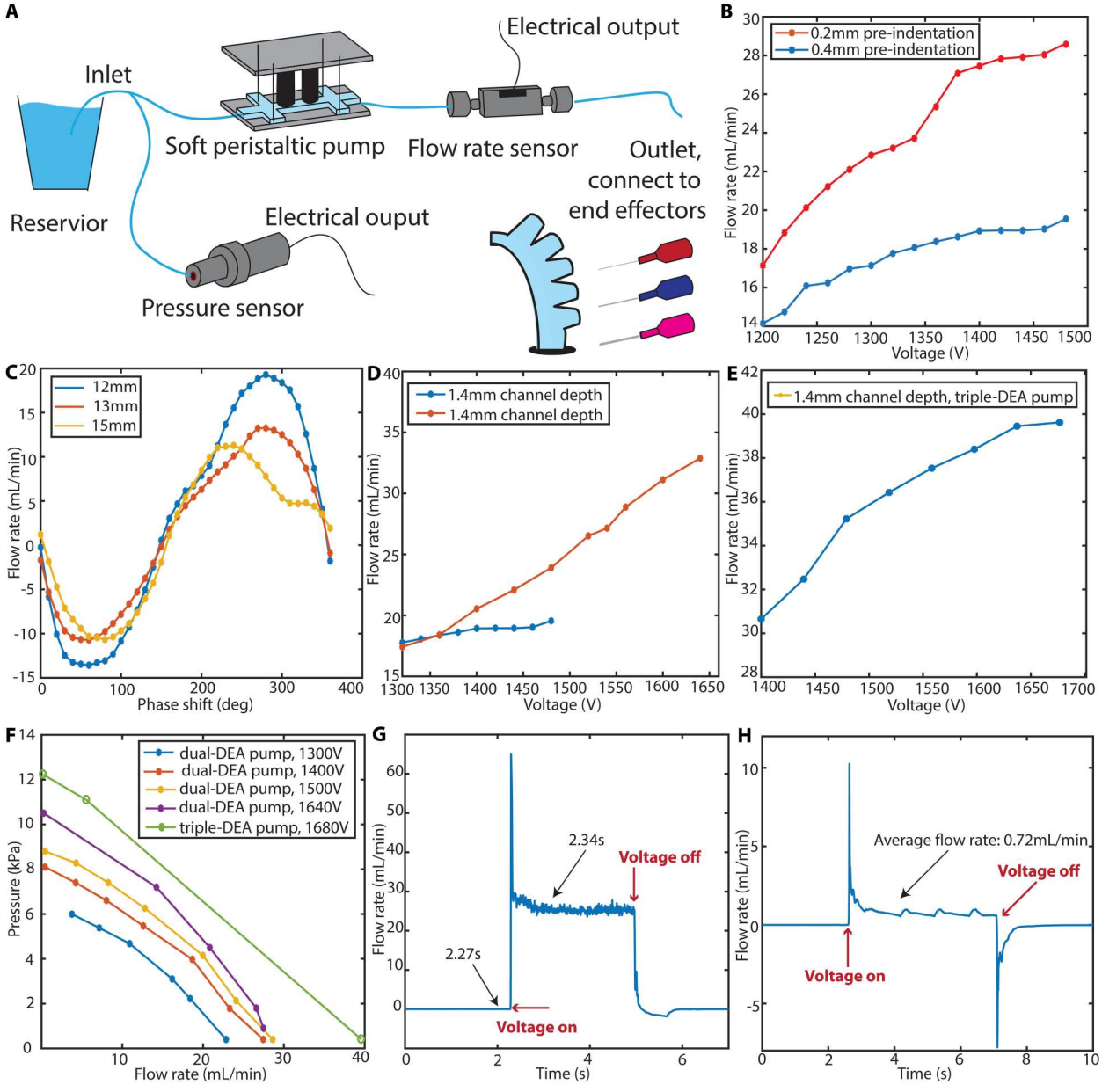

Fig. 4. Peristaltic pump performance characterization. The pump was operated at resonance with a 290° phase shift in all conditions if not otherwise stated. (**A**) Schematic of the fluidic circuit setup for pump characterization. (**B**) Measured average flow rate as a function of input voltage at two pre-indentation depths with a dual-DEA pump. (**C**) Measured average flow rate as a function of phase shift at three DEA separation distances. The pump was operated at 1400 V. (**D**) Influence of channel depth on the pump performance. In both conditions, the pre-indentation was 0.4 mm. (**E**) Measured average flow rate of a triple-DEA pump at various voltages with a 1.4-mm channel depth and a 0.4-mm pre-indentation. (**F**) Run-out flow rate and blocked pressure as a function of the voltage of a dual-DEA pump and the optimal performance achieved with a triple-DEA pump. For the dual-DEA pump, the channel depth was 1.2 mm, and the pre-indentation was 0.2 mm. For the triple-DEA pump, the channel depth was 1.4 mm, and the pre-indentation was 0.4 mm. (**G** and **H**) Flows generated by a dual-DEA pump operated at 1400 and 1000 V. The outlet resistance of (G) is negligible. The outlet needle diameter in (H) is about one-tenth of the channel diameter.

lower height, which reduced the volume of the working liquid underneath the DEAs. Intuitively, the flow rate is related to the volume of liquid transferred to the channel outlet per unit time, and a smaller volume leads to a lower flow rate. To verify this assumption, we tested a dual-DEA pump's flow rate with an indentation of 0.2 and 0.4 mm at various voltages and a phase shift of 290°. As shown in Fig. 4B, the pump with a 0.2-mm pre-indentation delivered more volumetric flow than the pump with a 0.4-mm pre-indentation. As the driving voltage increased from 1200 to 1500 V, the flow rate increased by approximately 60%, from 17.1 to 28.6 ml min^{-1}. This flow rate improvement was close to our expectation, given the square law between the DEA blocked force and electric field based on the Maxwell stress equation. Each data point in Fig. 4B is the average flow rate for at least 0.5 s (2-kHz sampling rate)

after transient startup behaviors have passed. In comparison, the pump with a 0.4-mm pre-indentation could generate 14 ml min^{-1} at 1400 V and only reached 19.5 ml min^{-1} at 1480 V. Although a lower pre-indentation provided a higher flow rate, it also increased the possibility of misalignment during the oscillation. The DEA was likely to detach from the channel surface with insufficient pre-indentation, which might further lead to mechanical failure of the system.

With a dual-DEA pump, we explored variation in the flow rate under different DEA separations and phase shifts and then compared the experimental results with the model prediction that we introduced in the previous section. We set one of the DEAs to be at zero phase as a reference and drove the second with the selected phase shift. The run-out flow rate was then measured as a function of phase shift from 0° to 360° in 10° increments (Fig. 4C). As we varied the phase shift, the time difference between the DEAs compressing the soft channel was varied accordingly. When this time difference matched the ratio of the distance between the DEAs to the wave speed, the flow rate reached its maximum. In other conditions, the motion of the second DEA partially blocked the forward liquid movement generated by the first DEA, thus reducing the flow rate. At 1400 V and a DEA separation of 12 mm, the pump reached its maximum forward and reverse flow rate at 290° and 60°, respectively. A demonstration of the bidirectional flow is shown in fig. S8 and movie S4. The DEA positions were symmetric with respect to the center of the channel. As the DEA separation distance was increased from 12 to 13 and 15 mm, the peak flow rates occurred at lower phase shifts, and the magnitude of the peak decreased. This trend agreed with the simulation predictions in Fig. 3C; however, variations in the experimental results were more pronounced. As the DEAs were moved apart, they got closer to the edge of the channel. A simplified open boundary condition was applied to the outlet in the simulation, but the molded silicone channel in our experiments had a channel-to-tubing connection region. Impedance changes in this region caused reflections that interfered with the forward traveling wave, thus reducing the measured peak flow rate. Interference from the channel edge also caused a phase shift at which the peak flow occurred, and a secondary peak could be observed at 15-mm separation. Following this trend, we could expect a higher flow rate when the DEA separation is further reduced to 10 mm. However, reducing the distance would increase the difficulties during pump assembly because of the dimension of the DEAs. Therefore, we selected a separation of 12 mm and phase shift of 290° as the design parameters for the following experiments and demonstrations.

In addition to pre-indentation and DEA separation, the channel depth is also an important factor. From the measurements of flow rate as a function of pump driving voltage in Fig. 4B, as the voltage increased to 1500 V, the increment of the flow rate gradually decreased and tended toward saturation. Although the DEAs could be operated up to 1700 V, little improvement in the pump flow rate could be observed after 1400 V. We believe that this behavior was due to the channel depth. As we increased the driving voltage, the DEA stroke increased until it touched the bottom surface of the channel. Further increasing the voltage no longer notably contributed to the flow rate and would induce buckling during the collision. To improve the pump performance, we increased the channel depth to 1.4 mm. Although little flow rate improvement occurred below 1360 V, the pump can be safely driven up to a much higher voltage (Fig. 4D). The maximum flow rate with a 1.4-mm depth was increased by approximately 68% compared with the previous case, reaching 33.9 ml min^{-1} at 1640 V.

The number of DEAs in the soft pump was another critical factor for pump behavior. From the model prediction (fig. S7), adding DEAs to the pump improved the outflow rate as more fluid volume was conveyed within one operation period. However, this increment was reduced as more DEAs were included and eventually reached saturation when the number of DEAs was large enough to generate a continuous wave. A triple-DEA pump could improve the flow rate by 16% compared with a dual-DEA pump, but a four-DEA pump only increases the flow rate by 7% relative to a triple-DEA pump. In addition, the fabrication process wouldl become substantially more complicated with additional actuators. Considering the pump efficiency and fabrication complexity, we explored the performance of a triple-DEA pump and compared it with that of a dual-DEA pump, maintaining all other parameters. From Fig. 4E, the triple-DEA pump generated a flow rate of 30.6 ml min^{-1} at 1400 V, approximately 50% higher than that of a dual-DEA pump. To explore the relationship between the flow rate and pressure, blunt needle tips were connected to the outlet, and the flow resistance could be tuned by adjusting the needle gauges. When the needle's inner diameter was similar to the channel diameter, the resistance was negligible, and little pressure change was detected within the fluidic circuit. We selected different needle gauges and characterized the pump's blocked pressure as a function of run-out flow rate at various voltages. As shown in Fig. 4F, both blocked pressure and flow rate grew as the voltage increased, and a triple-DEA pump outperformed a dual-DEA pump in both metrics. The triple-DEA pump with a 1.4-m channel and 0.4-mm pre-indentation depth had a maximum run-out flow rate of 39 ml min^{-1} and blocked pressure of 12.5 kPa at 1680 V. We estimated the triple-DEA pump efficiency on the basis of the fluidic power (half of the product of run-out flow rate and blocked pressure) and the electrical power consumption to be approximately 0.12%. Our soft pump exhibited an efficiency comparable to other types of soft pumps developed in previous research (*24*, *35*). Although there is currently a gap in performance between the DEA peristaltic pumps and off-the-shelf solenoid pumps, there are several ways to improve the pump's efficiency, including reducing the operating frequency and the electrode resistance, incorporating charge recovery circuitry in the drive electronics (*49*), and exploring low-viscoelasticity channel materials to reduce energy loss in deforming the channel.

By tuning the driving voltage and outlet resistance, the pump could generate microfluidic droplets with a flow rate of 720 μl min^{-1} at 1000 V. The pump exhibited quick responses (in less than 0.1 s) to changes in drive conditions (Fig. 4, G and H; fig. S9; and movie S5). The electrically controllable flow rate and pressure allowed the pump to function as both a power source and a valve (*45*, *48*), which led to fast and accurate control of the end effector of the fluidic system. We will leverage this capability in the following section.

Pumping of various liquids

The working fluid in a peristaltic pump only contacted the interior of the channel, which minimizes concerns of compatibility with the pump components and prevents liquid contamination. This property enabled peristaltic pumps to work with thick liquids, liquid suspensions, or shear-sensitive fluids (blood) and could be used in a

variety of applications, including handling of biomedical liquids, liquid dispensing for food service, and wearable thermal regulation devices. The viscosity of the working liquid was a major factor in the pump's performance. Intuitively, fluids with higher viscosity had a greater impedance compared with those with lower viscosity and thus were more difficult to transport under the same operating conditions. To investigate our pump's ability to manipulate the flow of various liquids, we first simulated the flow rate as a function of the liquid viscosity of a triple-DEA pump using the finite element analysis (FEA) model introduced in the previous section (Fig. 5A). Several commonly used represented fluids were selected as examples. The viscosity values were based on past characterization (*28*, *50*–*54*). We set the pump operation condition to be 1500 V with a phase shift of 290° at resonance and compared the average flow rate of each liquid.

From the simulation results, an exponential decay occurred in flow rate as the fluid viscosity increased from 0.89 to 200 cP. Observing the cumulative flow rate within each cycle (fig. S7), while the backward flow rate decreased as the viscosity increased, the net outflow was still reduced. If the viscosity increased far beyond 200 cP, then the flow rate would gradually approach zero.

To validate the model prediction and demonstrate compatibility with various fluids, we experimentally tested six common liquids using the triple-DEA pump: gin, water, lime juice, pineapple juice, coconut milk, and maple syrup (Fig. 5, B to E). The flow rate sensor was calibrated for each liquid before the measurement, and the results are elaborated in fig. S10. From Fig. 5B, the measured flow rate follows a similar trend with the simulation results as the fluid viscosity increases but with a faster decay. A continuous flow was observed when pumping water with a flow rate of 35 ml min^{-1}, whereas only droplets of maple syrup were generated at 0.25 ml min^{-1}, much lower than the simulated value (Fig. 5C). This was likely due to the energy loss at the channel connections. In the experiment setup, a 45-cm tube was connected to the channel inlet, whereas only the 5-cm soft channel was considered in the model. The energy loss within the long tube was greater for a high-viscosity

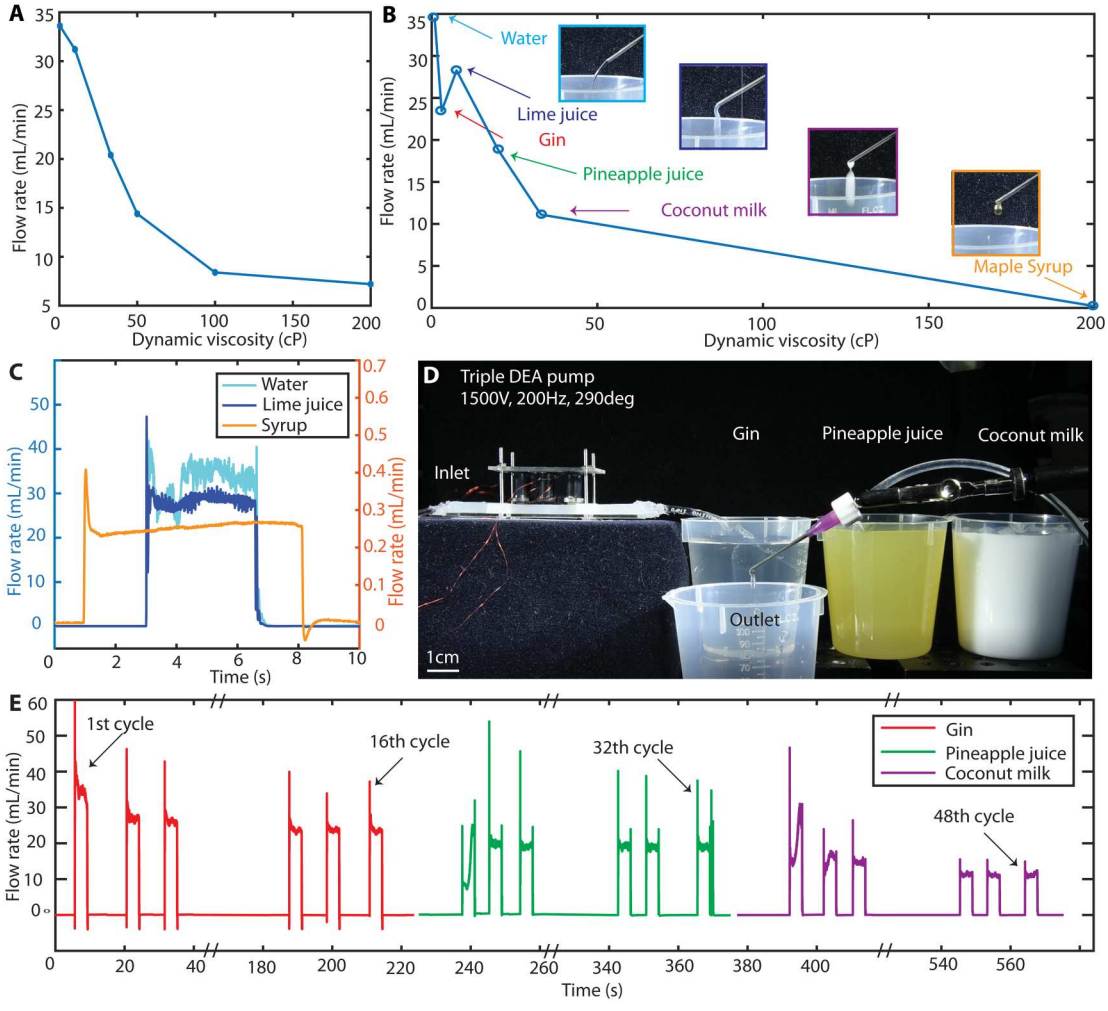

Fig. 5. Demonstration of the peristaltic pump delivering various liquids. All experiments were conducted with a triple-DEA pump operated at resonance at 1500 V and a 290° phase shift. (**A**) Model predictions of the run-out flow rate as a function of liquid dynamic viscosity for a triple-DEA pump. (**B**) Average flow rate of commonly used liquids with various viscosities. The inset pictures with light blue, navy, purple, and orange frames show the outflow when pumping water, lime juice, coconut milk, and maple syrup, respectively. (**C**) Real-time measured flow rate of water, lime juice, and syrup. (**D**) Setup for making a gin-based piña colada with our peristaltic pump. (**E**) Measured flow rate during the making of the drink. The pump was operated for 5-s intervals and repeated a total of 48 times. Scale bar, 1 cm.

liquid than a low-viscosity liquid. Therefore, the flow rate tended to decrease faster as the viscosity increased in our experiments.

To test the lifetime of the pump, we mixed a piña colada with the recipe of 20 ml of gin, 20 ml of pineapple juice, and 15 ml of coconut milk (Fig. 5, D and E, and movie S6). We operated the pump for 5 s and repeated the operation 48 times (16 times for each liquid) until the target volume was reached. There is a transient period at the beginning of each liquid delivery phase (the first one or two actuation periods). The transient period could be caused by the induced air bubbles and the liquid viscosity variation when loading and switching the working liquids. The flow rate of the first and last three operations of each liquid are shown in Fig. 5E. The cumulative operation time was approximately 85 s, and the pump performed consistently during this process.

Control of a bellows-shaped bending actuator and haptic devices

Our DEA pump was capable of powering and controlling fluidic actuators. To demonstrate this capability, we first fabricated a bellows-shaped actuator on the basis of prior designs (*45*, *48*) and connected it to the outlet of the pump. The actuator was made from Ecoflex 0030 silicone (Smooth-On), and its actuation volume, from the rest to maximum deformation, was approximately 4 ml. When the actuator was at rest, it was in a vertical neutral position (Fig. 6A). The bending angle and actuation time constant were determined by the operation pressure, the actuator stiffness, and the actuation volume. We pressurized the actuator from this rest position with our DEA pump under various driving voltages. An increase in the internal pressure caused the flow to decrease. We drove the actuator until we observed a decrease in flow rate of at least 90% after approximately two time constants and then released it to the initial position (Fig. 6, B and C). The working fluid flowed back to the reservoir under ambient pressure and gravity when the pump was turned off. This pressure release process could be accelerated by operating the pump in reverse. The instantaneous pressure and flow rate during the pumping and releasing process were recorded using pressure and flow rate sensors. Taking the 1640-V operating condition as an example, when a voltage was applied, the pump reacted within 0.1 s and generated an initial flow rate of 38 ml min^{-1} depending on the operation voltage. At the same time, the internal gauge pressure began to increase from 0 kPa. As the pressure gradually approached the pump blocked pressure, the flow rate approached zero and the actuator stopped moving. We defined the bending angle as the angle between a fixed line passing through the base of the actuator and its tip when at rest and at a specific measurement time. With a 1640-V electrical input, the bellow actuator achieved a maximum of 71° (fig. S12 and movie S7).

To determine the time constant of the hydraulic circuit, we drew an analogy to a first-order RC circuit. The flow rate and pressure change within the fluidic system were analogous, respectively, to the current and voltage variation during charging and discharging of the capacitor. We applied exponential fits to the measured flow rate and estimated the time constant on the basis of the fitted coefficients (fig. S12). The average time constant under 1680-, 1640-, 1580-V operation was approximately 2.5 s, with an SD of 0.3 s. On the basis of the pressure measurement in Fig. 6C, we determined that the actuator required more than 5 s to approach its maximum bending position, and the bending speed could not exceed 10° s^{-1}. This time constant and speed limit served as a guide when designing trajectories and closed-loop controllers for soft actuators controlled by the proposed DEA pump.

The peristaltic pump was able to tune its output pressure and flow on the basis of the electrical input without requiring additional valves. With this property, we demonstrated closed-loop control of a hydraulic actuator with a PI controller (Fig. 6, D and E). The motion of the actuator was controlled through adjustment of its internal pressure, as measured with a pressure sensor. As the system was operated, the pressure sensor sent feedback signals to the computer. The error between the target pressure and the measured pressure was sent to the PI controller, which tuned the voltage magnitude sent to the DEAs, thus controlling the pressure output of the pump. With this controller, we first experimentally validated the system time constant. On the basis of our previous open-loop test, the actuator required approximately 6 s to achieve a pressure of 8.1 kPa under 1600-V operation. We then designed three sinusoidal patterns with amplitudes of 8.1 kPa and different periods: 28, 24, and 20 s. The actuator was able to follow the trajectories with periods of 28 and 24 s but failed to track the 20-s trajectory. This agreed with the previous estimation and shows that the system requires a minimum of 6 s to stabilize during bending motion. With this time constant as a guideline for maximum bandwidth, we designed a complicated actuator bending motion trajectory including linear angle increase and decrease, pressure hold, and sinusoidal increases (Fig. 6D and fig. S12). A characterization test was performed that mapped the actuator bending angle to its internal pressure using a conventional hydraulic pump (JOVTOP-DC, JT-750) and valves (Enfield Technologies, PFV-W24-M100C-0400). Because of the dynamics of the soft actuator, we observed hysteresis in the mapping during the loading and unloading phases. For simplicity, we fit the relationship with a linear function and used it to convert target bending angles to the desired pressure. A comparison between the measured pressure and the target pressure of three trajectories is also shown in Fig. 6D. The root mean square error between the target and measured pressures was calculated to be 0.37 kPa. Because of the hysteresis, a latency in the bending motion was observed when comparing the tracked angle and desired trajectory, with an RMSE of 4.68° (fig. S12 and movie S7). The RMSE calculation did not include the transition period and was only measured for steady state. This result demonstrated both reliable power and control of a fluidic soft actuator with our DEA pump.

In addition to a bellows actuator, we also demonstrated control of custom soft actuators that could be used in haptic devices (Fig. 6, F and G, and movie S8). Two circular, silicone-molded, hydraulic actuators were designed on the basis of rigid, off-the-shelf actuators used in recent haptics research (*55*, *56*). Each actuator contained a circular actuation chamber with a diameter of 20 mm and depth of 6 mm. The two actuators were connected to the two ends of the soft pump, forming a closed fluidic system. The chambers were preloaded with water such that the elastomer membranes of the left and right actuators had an initial deformation of approximately 1 mm. By tuning the phase shift when operating the pump, we could transfer the liquid to either the left or the right actuator, causing the actuators to expand (Fig. 6F). We recorded the fluid flow rate and a video of the motion of the membranes during actuation, which we subsequently tracked. The tracked motions are shown in Fig. 6G.

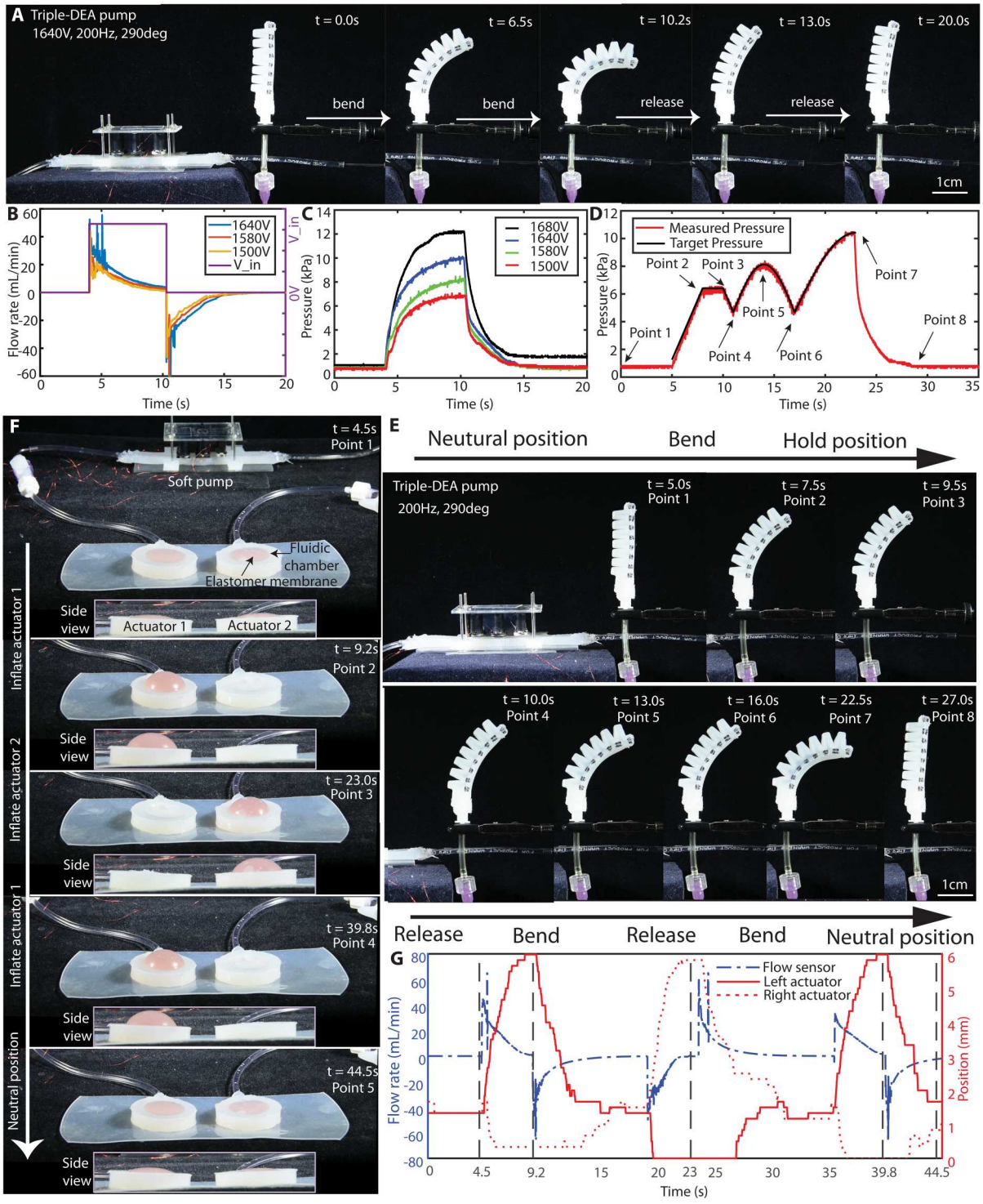

Fig. 6. Demonstration of the peristaltic pump powering and controlling a bellows actuator and a fluidic haptic actuator. (**A**) Bending motion of a bellows actuator when driving the pump at 1640 V and a phase of 290° at resonance. (**B**) Electrical input and flow rate responses when driving the bellows actuator at various voltages at resonance. (**C**) Pressure responses when driving the bellows actuator at various voltages at resonance. (**D**) Closed-loop pressure tracking performance. (**E**) Bending motion of the hydraulic actuator when controlled to follow the trajectory in (D). (**F**) Top and side views of the responses of two custom haptic actuators driven by the soft pump. (**G**) Flow rate responses and tracked motions of the two haptic actuators shown in (F). Scale bar, 1 cm.

The actuators were inflated in the sequence of left-right-left. Actuation started at 4.5 s with the pump moving water from the right actuator to the left one and then releasing to the initial conditions under ambient pressure. This could be seen from the positive flow rate measured at 4.5 s, which gradually reached zero when all the liquid was moved to the left actuator. At this time (9.2 s), the maximum inflation (vertical displacement) of 6 mm in the left actuator was reached, and a low pressure region was created in the right actuator. When the pressure was released after 9.2 s, a reverse flow occurred, and the inflated membrane in the left actuator relaxed to its initial condition. This process was repeated to inflate the right actuator then the left actuator again, and similar results were observed from the tracking results and the flow rate measurement.

Biggs and Srinivasan (*57*) showed that normal force applied to the forearm by a circular tactor 1 mm in diameter with 1.5 mm of skin indentation at 1 Hz could consistently and accurately be perceived by a user. Thus, the normal force from the vertical displacement of the actuator membrane generated by the fluid flow from the pump could be used to generate the desired haptic sensations. We envision that this system could be worn on a user′s forearm and provide a soft, comfortable alternative to traditional rigid wearable haptic devices.

DISCUSSION

In this work, we demonstrated a DEA-based, centimeter-scale soft linear peristaltic pump with a millimeter-sized channel for generating and controlling flow. The driving conditions of the pump, specifically the frequency and phase shift, were tuned to match the designed distance between the DEAs. The combined motion of the DEAs created a propagating peristaltic wave on the channel wall, driving the internal liquid in a specified direction. With a finite element multiphysics model, we investigated the influence of channel height, pre-indentation depth, DEA separation, and number of DEAs on the peristaltic pump′s fluidic power output. We demonstrated promising performance of the pump creating bidirectional flow up to 39 ml min^{-1} and a maximum blocked pressure of 12.5 kPa with a response time less than 0.1 s. We also demonstrated compatibility of the pump with a variety of working liquids that have different dynamic viscosities. In addition, the pump allowed precise control of hydraulic actuators in a valveless fluidic system.

Although previous work has introduced centimeter-sized soft pumps for hydraulic actuators, none addressed the challenges of peristaltic pumping mechanisms at this scale. To construct a propagating wave, forces from the actuators were applied to deform the channel in an arranged pattern. The actuator separation distance should match the product of the actuator operation frequency and wave propagation speed. In typical peristaltic pumps, rigid motors are used to compress the fluidic channels, but the weight, size, and maximum frequency of these actuators limit the scalability of such pumps. Our high power density and high bandwidth of 0.8-cm rolled DEAs provide the solution for small-scale peristaltic pumps. The high bandwidth allowed decent flow rates while maintaining a compact pump structure, with a DEA-to-channel contact area of only 4 mm by 5 mm. In addition, the high energy density of the DEAs provided sufficient force and stroke to the channel to achieve the target run-out flow rate and blocked pressure. Compared with existing soft peristaltic fluidic systems, our pump achieved three times higher pressure density and flow rate density. With our soft pump, we demonstrated reliable control of a bellows-shaped actuator and wearable haptic devices with similar sizes and weights as the pump, showing potential for onboard power systems for fluidic robots.

Although the pump has shown promising performance, there remain several aspects to optimize its design and functionality. Our design relied on cylindrical DEAs to provide sufficient pressure onto the channel. The height of the pump was dictated by the active height of the actuators. Low-profile DEA designs with similar power densities were required to reduce the thickness of the pump. In addition, the mechanical frame in the current design was made of rigid materials. The top and bottom plates could be potentially replaced by flexible materials, such as Sylgard 184 (Dow). The metal alignment pins could also be made of lighter materials, such as plastic. This would bring more flexibility to the pump and reduce its weight. Furthermore, to tune the resonance of the DEAs without notably reducing their output power and complicating the fabrication process, we added weight to the free end of the actuator, which doubled the overall weight of the DEA. The development of large-area DEAs with similar breakdown voltages and energy densities is necessary to improve the scalability and performance (i.e., specific pressure and flow rate) of the soft pump. Last but not least, the high voltage drive signal required the pump to be tethered, which currently limits its use in wearable devices or for untethered applications with a mobile robot. It is critical to reduce the driving voltage by reducing the layer thickness. Compact electronics and high energy density batteries are also necessary to achieve future generations of integrated power systems for fluidic robots.

MATERIALS AND METHODS

Soft pump fabrication and assembly

A soft pump contained two or three rolled dual-DEA structures, a soft channel, and a mechanical frame. A multilayer rolled DEA was fabricated through a process developed in a previous study (*44*). Each multilayer elastomer sheet was 104 mm long and 11 mm wide, and each rolled DEA had an active height of 9 mm. The multilayered sheet contained five functional elastomer layers (30-μm thickness) and two encapsulation layers (20-μm thickness), both made of Elastosil P7670 silicone. Each functional elastomer layer was sandwiched between two carbon nanotube electrode layers (Nano C) (fig. S1). A 250-mg weight was attached to one end of the rolled-DEA structure using conductive carbon adhesives. Two such rolled DEAs were combined in parallel into a dual-DEA structure. The indenter was three-dimensionally (3D) printed using a Stratasys Objet 30 printer and was glued to the DEA structure with adhesive. The indenter was 2 mm in height, 5 mm in length, and 4.5 mm in width, with a concave bottom surface matching the cross section of the fluidic channel. Each dual-DEA weighed 1.7 g.

The fluidic channel was cast with a 3D-printed mold. The mold contained a 5-cm-long and 4-mm-wide channel pattern. It also included 2-cm-long 0.5-cm-diameter cylindrical openings at the two ends of the channel to connect the channel to external tubing. The channel had a concave cross section and a depth of 1.2 or 1.4 mm. To fabricate the channel, we filled the mold with Dragon Skin 20 (Smooth-on Inc.) elastomer precursor and cured it at 70°C for 30 min. An elastomer layer was spin-coated on an acrylic substrate at

350 rpm for 1 min and cured under the same conditions. This cured layer was then spin-coated with a wet layer of the same material at 1500 rpm for 1 min. The cast channel was placed onto the wet layer and left at room temperature for 12 hours to bond the layers.

The top and bottom acrylic plates were manufactured with a laser cutter (Universal Laser Systems, VLS 6.75). The top plate was 5 cm long by 3 cm wide. The bottom plate was 9 cm long by 3 cm wide. To assemble the pump, the soft channel was first placed on top of the bottom acrylic plate. Four alignment pins (Mcmaster-Carr) connected the channel and plate through alignment holes. Then, the DEAs were aligned and attached to the top plate with Gel Pak adhesive (Gel-film, WF-40 × 40-0170-X8). Last, the top plate was aligned to the bottom plate through the pins, and ultraviolet adhesive was applied around the pin holes for stabilization.

DEA characterization setup

The DEA free displacement was measured with a high-speed camera (Phantom V1612) at 20,000 fps (fig. S4A). We operated the DEA for 0.5 s at frequencies ranging from 200 to 600 Hz in increments of 25 Hz. This process was repeated after adding weights to the actuator, with a frequency range from 80 to 300 Hz. Five hundred frames of the video taken at each frequency were saved, and the DEA motion was tracked every ten frames with a MATLAB script.

The force was measured using a Nano17 force sensor (ATI Industrial Automation) (fig. S4, B to D). To measure the preload force applied to the channel, a dual-DEA structure was attached to the end of the force sensor with Gel Pak. The sensor was screwed onto a micrometer tuning stage, and a fluidic channel was placed under the DEA, in contact with the pinch tip. The pre-indentation distance of the DEA into the channel was tuned by adjusting the height of the tuning stage. For blocked force measurements, we sandwiched the dual-DEA between the force sensor and a fixed substrate with the previously measured preload values. Voltages ranging from 1000 to 1700 V were applied with an increment of 50 V.

Demonstration experimental setup

The flow rate was measured with a flow sensor (Sensirion AG, SLF3S-0600F) connected in series with the soft pump. The data were recorded with USB RS485 Sensor Viewer software. The fluidic pressure was measured with a pressure sensor (TE Connectivity Measurement Specialties Inc., U5244-000005-005PG) connected in parallel with the soft pump, and the analog data were collected with a DAQ (National Instrument, USB-6008). The pump control system was built in Simulink and was modified on the basis of a previous precious study (*48*). To map the bellows-shaped actuator pressure to its bending angle, an off-the-shelf hydraulic pump (OVTOP JT-750) was used as the pressure source. A customized rigid valve for a previous fluidic soft actuator study was used for pressure regulation (*48*). Video of the haptic actuators was recorded with a camera (Nikon D7500). The motion of the actuators was manually post-processed in MATLAB. We tracked the center points of each actuator, as can be seen in movie S8.

Hydraulic bellows-style actuator and haptic actuator fabrication

The hydraulic bellows-shaped actuator was based on previous designs (*58*, *48*). The fabrication process involved casting and curing an inner soft core and the outer bellows shape with 3D-printed molds (fig. S13). The molds for each component contained two complimentary halves: one contained bellows structures, and one served as the inverse substrate. Two supporting rods with a diameter of 0.5 mm were comolded with the inner core to support and aligned the core the subsequent molding process. Both halves of the core mold were then filled with M4601 elastomer (Wacker Chemical), combined, and fixed with a clamp before curing at 70°C for 30 min in an oven. To fabricate the actuator, the inner core with an embedded supporting rod was aligned with the bellows structures in the mold. Ecoflex 0030 was then poured into both parts of the actuator and mold-cured in an oven at 70°C for 20 min. After curing, the inner core was pulled out of the actuator together with the rods. The holes at the top of the actuator from the supporting rods were sealed with Silpoxy adhesive (Smooth-On Inc).

The haptic actuator was also based on previous designs (*55*, *56*). The haptic actuator was manufactured through a cast, cure, and bonding process. The actuator chamber mold was laser-cut (Universal Laser Systems) from a 6.35-mm (1/4-inch) acrylic plate. It contained a substrate, a circular ring with an inner diameter of 15 mm and an outer diameter of 20 mm, and a circular disk with a diameter of 10 mm (same as the chamber diameter) (fig. S13). The three parts were glued together using double-sided tape. We filled the mold with Dragon Skin 20 elastomer (Smooth-On Inc) and cured it at 70°C for 20 min. The actuator substrate was spin-coated at 200 rpm for 60 s and bonded to the chamber through a wet bonding method.

Supplementary Materials

This PDF file includes:
Supplementary Text
Figs. S1 to S13
Tables S1 to S3

Other Supplementary Material for this manuscript includes the following:
Movies S1 to S8

REFERENCES AND NOTES

1. P. Polygerinos, Z. Wang, K. C. Galloway, R. J. Wood, C. J. Walsh, Soft robotic glove for combined assistance and at-home rehabilitation. *Rob. Auton. Syst.* **73**, 135–143 (2015).
2. L. Rosalia, C. Ozturk, J. Coll-Font, Y. Fan, Y. Nagata, M. Singh, D. Goswami, A. Mauskapf, S. Chen, R. A. Eder, E. M. Goffer, J. H. Kim, S. Yurista, B. P. Bonner, A. N. Foster, R. A. Levine, E. R. Edelman, M. Panagia, J. L. Guerrero, E. T. Roche, C. T. Nguyen, A soft robotic sleeve mimicking the haemodynamics and biomechanics of left ventricular pressure overload and aortic stenosis. *Nat. Biomed. Eng.* **6**, 1134–1147 (2022).
3. Y. Zhao, M. Hua, Y. Yan, S. Wu, Y. Alsaid, X. He, Stimuli-responsive polymers for soft robotics. *Annu. Rev. Control Robot. Auton. Systems* **5**, 515–545 (2022).
4. P. Polygerinos, N. Correll, S. A. Morin, B. Mosadegh, C. D. Onal, K. Petersen, M. Cianchetti, M. T. Tolley, R. F. Shepherd, Soft robotics: Review of fluid-driven intrinsically soft devices; manufacturing, sensing, control, and applications in human-robot interaction. *Adv. Eng. Mater.* **19**, 1700016 (2017).
5. N. R. Sinatra, C. B. Teeple, D. M. Vogt, K. K. Parker, D. F. Gruber, R. J. Wood, Ultragentle manipulation of delicate structures using a soft robotic gripper. *Sci. Robot.* **4**, eaax5425 (2019).
6. A. D. Marchese, D. Rus, Design, kinematics, and control of a soft spatial fluidic elastomer manipulator. *Int. J. Robot. Res.* **35**, 840–869 (2016).

7. R. Z. Gao, C. L. Ren, Synergizing microfluidics with soft robotics: A perspective on miniaturization and future directions. *Biomicrofluidics* **15**, 011302 (2021).
8. J. D. Hubbard, R. Acevedo, K. M. Edwards, A. T. Alsharhan, Z. Wen, J. Landry, K. Wang, S. Schaffer, R. D. Sochol, Fully 3D-printed soft robots with integrated fluidic circuitry. *Sci. Adv.* **7**, eabe5257 (2021).
9. M. Tschiersky, E. E. Hekman, D. M. Brouwer, J. L. Herder, K. Suzumori, A compact McKibben muscle based bending actuator for close-to-body application in assistive wearable robots. *IEEE Robot. Autom. Lett.* **5**, 3042–3049 (2020).
10. G. K. Klute, J. M. Czerniecki, B. Hannaford, in *1999 IEEE/ASME International Conference on Advanced Intelligent Mechatronics (Cat. No. 99TH8399)* (IEEE, 1999), pp. 221–226.
11. E. Acome, S. K. Mitchell, T. G. Morrissey, M. B. Emmett, C. Benjamin, M. King, M. Radakovitz, C. Keplinger, Hydraulically amplified self-healing electrostatic actuators with muscle-like performance. *Science* **359**, 61–65 (2018).
12. S. T. Mahon, A. Buchoux, M. E. Sayed, L. Teng, A. A. Stokes, 2019 *2nd IEEE International Conference on Soft Robotics (RoboSoft)* (IEEE, Korea, Republic of Seoul 14 to 18 April 2019), pp. 782–787.
13. T. Ranzani, S. Russo, N. W. Bartlett, M. Wehner, R. J. Wood, Increasing the dimensionality of soft microstructures through injection-induced self-folding. *Adv. Mater.* **30**, 1802739 (2018).
14. M. De Volder, D. Reynaerts, Pneumatic and hydraulic microactuators: A review. *J. Micromech. Microeng.* **20**, 043001 (2010).
15. N. Kellaris, V. Gopaluni Venkata, G. M. Smith, S. K. Mitchell, C. Keplinger, Peano-HASEL actuators: Muscle-mimetic, electrohydraulic transducers that linearly contract on activation. *Sci. Robot.* **3**, eaar3276 (2018).
16. D. McCoul, Q. Pei, Tubular dielectric elastomer actuator for active fluidic control. *Smart Mater. Struct.* **24**, 105016 (2015).
17. J. Hughes, U. Culha, F. Giardina, F. Guenther, A. Rosendo, F. Iida, Soft manipulators and grippers: A review. *Front. Robot. and AI* **3**, 69 (2016).
18. E. Q. Yumbla, Z. Qiao, W. Tao, W. Zhang, Human assistance and augmentation with wearable soft robotics: A literature review and perspectives. *Curr. Robot. Rep.*, 1–15 (2021).
19. S. I. Rich, R. J. Wood, C. Majidi, Untethered soft robotics. *Nat. Electron.* **1**, 102–112 (2018).
20. C. Stergiopulos, *Smart Materials, Adaptive Structures and Intelligent Systems* (American Society of Mechanical Engineers, 2014), vol. 46155, p. V002T04A011.
21. W. Michael, L. R. Truby, D. J. Fitzgerald, B. Mosadegh, G. M. Whitesides, J. A. Lewis, R. J. Wood, An integrated design and fabrication strategy for entirely soft, autonomous robots. *Nature* **536**, 451–455 (2016).
22. P. K. Das, A. T. Hasan, *AIP Conference Proceedings* (AIP Publishing LLC, 2017), vol. 1851, p. 020110.
23. J. Han, W. Jiang, D. Niu, Y. Li, Y. Zhang, B. Lei, H. Liu, Y. Shi, B. Chen, L. Yin, X. Liu, D. Peng, B. Lu, Untethered soft actuators by liquid–Vapor phase transition: Remote and programmable actuation. *Adv. Intell. Syst.* **1**, 1900109 (2019).
24. V. Cacucciolo, J. Shintake, Y. Kuwajima, S. Maeda, D. Floreano, H. Shea, Stretchable pumps for soft machines. *Nature* **572**, 516–519 (2019).
25. N. W. Bartlett, K. P. Becker, R. J. Wood, A fluidic demultiplexer for controlling large arrays of soft actuators. *Soft Matter* **16**, 5871–5877 (2020).
26. A. Zatopa, S. Walker, Y. Menguc, Fully soft 3D-printed electroactive fluidic valve for soft hydraulic robots. *Soft Robot.* **5**, 258–271 (2018).
27. J. Kestin, M. Sokolov, W. A. Wakeham, Viscosity of liquid water in the range −8 °C to 150 °C. *J. Phys. Chem. Ref. Data Monogr.* **7**, 941–948 (1978).
28. M. Ngadi, L. Yu, Textural and other quality properties of instant fried noodles as affected by ingredients. *Can. Biosyst. Eng.* **46**, 3.15 (2004).
29. Y. Chen, T.-H. Wu, P.-Y. Chiou, Scanning laser pulses driven microfluidic peristaltic membrane pump. *Lab Chip* **12**, 1771–1774 (2012).
30. S. Solano-Arana, F. Klug, H. Mößinger, F. Förster-Zügel, H. F. Schlaak, A novel application of dielectric stack actuators: A pumping micromixer. *Smart Mater. Struct.* **27**, 074008 (2018).
31. K. S. Lee, B. Kim, M. A. Shannon, An electrostatically driven valve-less peristaltic micropump with a stepwise chamber. *Sens. Actuators A Phys.* **187**, 183–189 (2012).
32. B. T. Chia, H.-H. Liao, Y.-J. Yang, A novel thermo-pneumatic peristaltic micropump with low temperature elevation on working fluid. *Sens. Actuators A Phys.* **165**, 86–93 (2011).
33. Z. Li, Y. Wang, C. C. Foo, H. Godaba, J. Zhu, C. H. Yap, The mechanism for large-volume fluid pumping via reversible snap-through of dielectric elastomer. *J. Appl. Phys.* **122**, 084503 (2017).
34. C. Cao, X. Gao, A. T. Conn, A magnetically coupled dielectric elastomer pump for soft robotics. *Adv. Mater. Technol.* **4**, 1900128 (2019).
35. T. Wang, W. Shao, Z. Huang, H. Tang, J. Zhang, Z. Ding, K. Huang, *Nat. Commun.* **12**, 3445 (2021).
36. Y. Matia, H. S. An, R. F. Shepherd, N. Lazarus, Magnetohydrodynamic levitation for high-performance flexible pumps. *Proc. Natl. Acad. Sci. U.S.A.* **119**, e2203116119 (2022).
37. F. Esser, T. Masselter, T. Speck, Silent pumpers: A comparative topical overview of the peristaltic pumping principle in living nature, engineering, and biomimetics. *Adv. Intell. Syst.* **1**, 1900009 (2019).
38. K. B. Vinayakumar, G. Nadiger, V. R. Shetty, N. S. Dinesh, M. M. Nayak, K. Rajanna, Packaged peristaltic micropump for controlled drug delivery application. *Rev. Sci. Instrum.* **88**, 015102 (2017).
39. G. Shi, A. Palombi, Z. Lim, A. Astolfi, A. Burani, S. Campagnini, F. G. C. Loizzo, M. L. Preti, A. M. Vargas, E. Peperoni, C. M. Oddo, M. Li, J. Hardwicke, M. Venus, S. Homer-Vanniasinkam, H. A. Wurdemann, Fluidic haptic interface for mechano-tactile feedback. *IEEE Trans. Haptics* **13**, 204–210 (2020).
40. E. Foo, J. Baker, C. Compton, B. Holschuh, *Extended Abstracts of the 2020 CHI Conference on Human Factors in Computing Systems* (2020), pp. 1–8.
41. M. Jaffrin, A. Shapiro, Peristaltic pumping. *Annu. Rev. Fluid Mech.* **3**, 13–37 (1971).
42. K. Suzuki, T. Nakamura, *2010 IEEE/RSJ International Conference on Intelligent Robots and Systems* (IEEE, Taipei, Taiwan, 18 to 22 October 2010), pp. 3085–3090.
43. M. Zhu, W. Xu, L. K. Cheng, *IEEE/ASME Trans. Mechatron.* **22**, 91 (2017).
44. H. Zhao, A. M. Hussain, M. Duduta, D. M. Vogt, R. J. Wood, D. R. Clarke, Compact dielectric elastomer linear actuators. *Adv. Funct. Mater.* **28**, 1804328 (2018).
45. S. Xu, Y. Chen, N.-S. P. Hyun, K. P. Becker, R. J. Wood, A dynamic electrically driven soft valve for control of soft hydraulic actuators. *Proc. Natl. Acad. Sci. U.S.A.* **118**, e2103198118 (2021).
46. J. Pfitzner, Poiseuille and his law. *Anaesthesia* **31**, 273–275 (1976).
47. E. Y. Wu, J. Sune, W. Lai, On the weibull shape factor of intrinsic breakdown of dielectric films and its accurate experimental determination-part II: Experimental results and the effects of stress conditions. *IEEE Trans. Electron Devices* **49**, 2141–2150 (2002).
48. J. Poccard-Saudart, S. Xu, C. B. Teeple, N. S. P. Hyun, K. P. Becker, R. J. Wood, Controlling soft fluidic actuators using soft DEA-based valves. *IEEE Robot. Autom. Lett.* **7**, 8837–8844 (2022).
49. J.-P. L. Bigué, J.-S. Plante, Experimental study of dielectric elastomer actuator energy conversion efficiency. *IEEE/ASME Trans. Mechatron.* **18**, 169–177 (2013).
50. L. Korson, W. Drost-Hansen, F. J. Millero, Viscosity of water at various temperatures. *J. Phys. Chem.* **73**, 34–39 (1969).
51. S. O. Essien, E. U. Usoh, Effect of themerature on the rheological properties of pineapple juice (Ananas comosus). *Int. J. Res. Sci. Eng.* **5**, 86–90 (2016).
52. RheoSenselnc, *Viscosity of Two Component Mixtures*.
53. K. Khuenpet, W. Jittanit, N. Hongha, S. Pairojkul, UHT skim coconut milk production and its quality. *Sciences* **23**, 03002 (2016).
54. W. Jittanit, N. Suriyapornchaikul, S. Nithisopha, The comparison between the quality of lime juices produced by different preservation techniques. *Procedia Soc. Behav. Sci.* **91**, 691–696 (2013).
55. H. Culbertson, *et al.*, *IEEE Haptics Symposium (HAPTICS)* (IEEE, San Francisco, California, 25 to 28 March 2018), pp. 32–39.
56. C. M. Nunez, B. N. Huerta, A. M. Okamura, H. Culbertson, Investigating social haptic illusions for tactile stroking (SHIFTS), *IEEE Haptics Symposium (HAPTICS)* (IEEE, Crystal City, VA, USA, 28 to 31 March 2020), pp. 629–636.
57. J. Biggs, M. A. Srinivasan, *Proc. Symposium on Haptic Interfaces for Virtual Environment and Teleoperator Systems* (2002), pp. 121–128.
58. K. C. Galloway, K. P. Becker, B. Phillips, J. Kirby, S. Licht, D. Tchernov, R. J. Wood, D. F. Gruber, Soft robotic grippers for biological sampling on deep reefs. *Soft Robot.* **3**, 23–33 (2016).

Acknowledgments: We would like to thank M. Yuen for discussions and proofreading. **Funding:** This work is supported by the National Science Foundation (award no. CMMI-1830291). Any opinions, findings, and conclusions or recommendations expressed in this material are those of the authors and do not necessarily reflect the views of the National Science Foundation. **Author contributions:** S.X. and R.J.W. proposed and designed the research. S.X. designed the device and performed the experimental work. S.X. and C.M.N. analyzed the data. S.X. and M.S. developed the finite element model. S.X., C.M.N., and R.J.W. wrote the paper. All authors provided feedback. **Competing interests:** This work is protected by U.S. Provisional Application No. 63/441,040 (provisional application title: "Compact peristaltic pump based on dielectric elastomer actuator") filed 25 January 2023. The authors declare that they have no other competing interests. **Data and materials availability:** All data are available in the main text or the Supplementary Materials. Data are also available on Dryad (DOI 10.5061/dryad.x0k6djhj1).

Submitted 19 October 2022
Accepted 24 May 2023
Published 21 June 2023
10.1126/scirobotics.add4649

Science Robotics

A compact DEA-based soft peristaltic pump for power and control of fluidic robots

Siyi Xu, Cara M. Nunez, Mohammad Souri, and Robert J. Wood

Sci. Robot. **8** (79), eadd4649. DOI: 10.1126/scirobotics.add4649

Science Robotics (ISSN 2470-9476) is published by the American Association for the Advancement of Science. 1200 New York Avenue NW, Washington, DC 20005. The title *Science Robotics* is a registered trademark of AAAS.